A multi-spectral compact local geometric distortion measurement setup based on a two-axis rotation camera

L. Greusard[a], V. Brinster[a], I. Salihi[a], A. Bertaud[a], C. Barrat*[a]
[a]HGH Systèmes Infrarouges, 10 Rue Maryse Bastié, 91430 Igny, France

ABSTRACT

Characterizing the quality parameters of imagers such as the optical distortion is a key point for applications such as defence and security, especially for wide-angle systems. Here, we developed a compact setup using pinhole image projected by a mirror-based off-axis collimator in front of the unit under test (UUT). The former is fixed while the latter is mounted on a 2-axis rotation platform. The collimator projects at infinity a pinhole while the UUT rotates, allowing a perfectly controlled imaging on the desired area. Here, we present this system and the postprocessing method correcting the rotation of the UUT, allowing to reach a top-notch measurement accuracy. Our setup has been successfully deployed and can be used for visible imagers or thermal imagers by easily switching the source (blackbody or integrating sphere) set to the collimator.

Keywords: Optical distortion, off-axis collimator, infrared imagers, visible cameras, infrared seeker, multi-spectral testing

1. INTRODUCTION

Wide-field-of-view optronic systems are extensively used in defence (countermeasures), security, and aerial mapping applications, necessitating minimal distortion levels for optimal performance [1-3]. Accurate characterization of optical distortion is essential in refining the overall optronic system. Traditional distortion measurement techniques rely on rectangular dot charts or structured patterns, as standardized in ISO 90931 [4] and ISO 17850 [5]. Alternative methods such as mathematical modelling [6,7], Moiré interferometry, and diffractive optics [8-11] exist but often present limitations, including narrow spectral bandwidths, extensive time requirements, and large experimental setups.

This paper introduces a fully operational multispectral compact distortion test bench optimized for production environments. The system is designed to minimize spatial footprint while accommodating wide-angle imaging systems operating from visible to long-wave infrared (LWIR) wavelengths.

Section 2 details the test bench design and measurement procedure, including post-processing corrections. Section 3 outlines the crucial correction method integrated into the system. Measurement uncertainties are quantified in Section 4, while Section 5 extends the methodology to distortion measurements through optical windows placed in front of the UUT.

*catherine.barrat@hgh-infrared.com

2. DISTORTION BENCH AND MEASUREMENT PROCEDURE

The principle of our distortion bench is to project a hole at various angles of the field of view of the UUT and to compare the actual position of the hole image on the UUT matrix versus the theoretical position given by the angles. The major contribution of this bench is that the collimator, usually a heavy structure, does not move while the UUT rotates, thus scanning its entire field of view.

The developed distortion measurement system consists of a mirror-based off-axis collimator with a pinhole pattern at its focal point, mounted on a motorized target wheel. The collimator has a focal length ranging from 750 mm to 3000 mm, with mirror diameters between 150 mm and 400 mm, the diameter selection depending on the aperture of the UUT. A light source positioned behind the pinhole pattern serves as an illumination source, configurable as either:

- A blackbody for infrared applications (e.g., temperature-compensated blackbody HGH DCN1000H4 [12]).
- An integrating sphere-based source for visible and short-wave infrared (SWIR) applications (e.g., HGH ISV210-F or ISV410 [13]).

The UUT is positioned in front of the collimator output, mounted on a two-axis motorized rotation stage. The different elements are controlled with our INFRATEST® software (for instance, a Newport goniometer M-BGM120BPP a Newport 360° motorized rotation stage URS100BPP controlled through a Newport ESP302-2N controller).

The conception of this bench is high precision driven. As the accuracy of the measurement depends on the accuracy of the rotation stages (see Section 4), the stages of our bench were selected to have high accuracy of positioning leading to a limited payload. A compromise has to be taken between the payload and the accuracy when selecting the stages.

Hence, whatever the angle of rotation, the projected image of the pinhole is aberration-free.

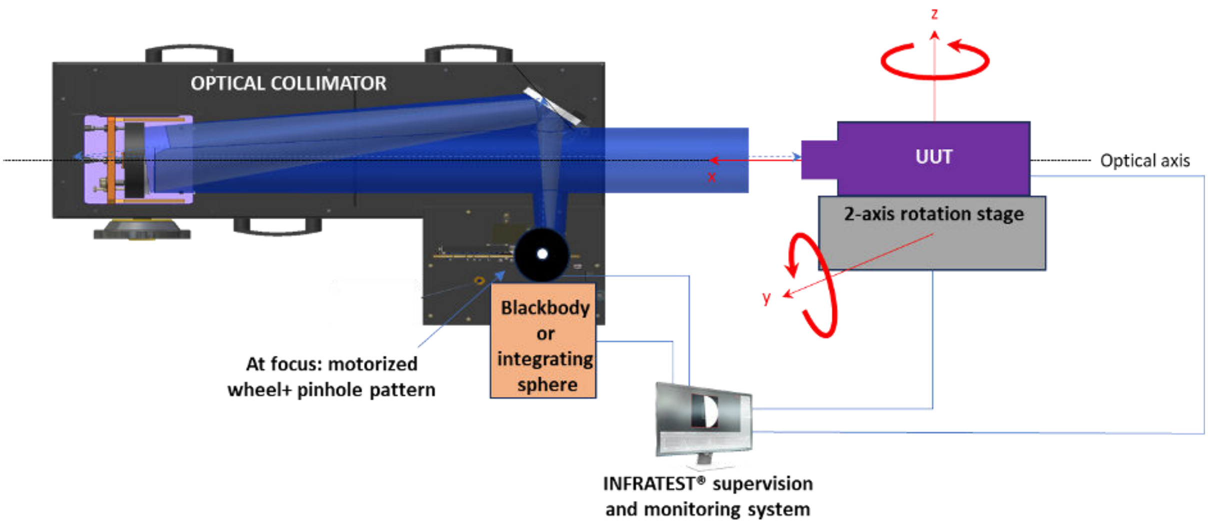

Figure 1. Schematics of the distortion test bench. The collimated radiation emitted from a very fine-controlled source radiation through an off-axis parabolic mirror-based collimator, is focused on the UUT. The UUT is mounted on a motorized 2-axis rotation stage. All motorized components, the source and the UUT are monitored or controlled with the same INFRATEST® software.

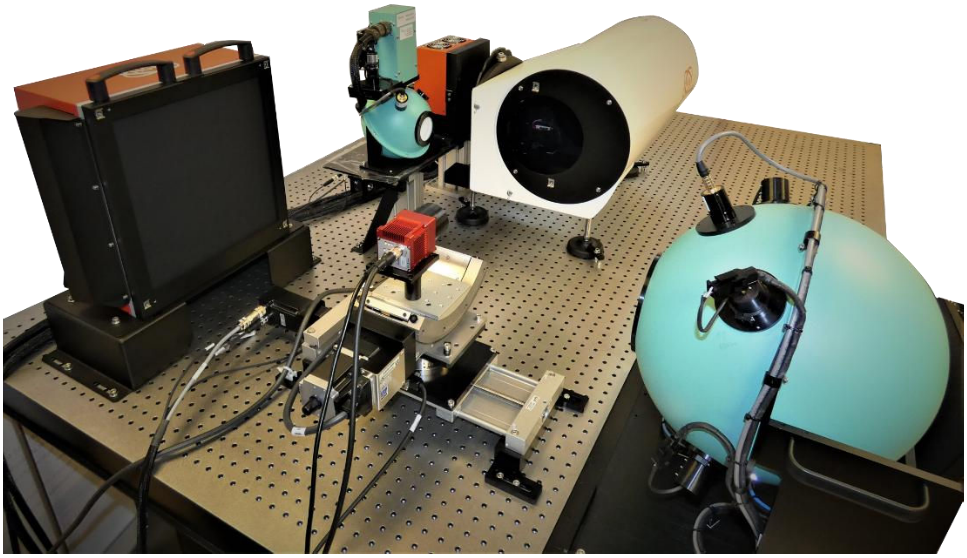

Figure 2. Example of motorized bench for distortion measurement

The distortion measurement procedure follows these steps:

1. **Calibration**: Identifying azimuth and elevation values required to project the pinhole image at the image's edges.
2. **Automated Scan**: The azimuth and elevation steps and the number of averaged frames are specified by the operator. The system automatically moves the azimuth & elevation motors, thus orienting the UUT so that the pinhole is projected at various positions on the FPA (Focal Plane Array). Then it acquires N frames and automatically places the same ROI (Region of Interest) around the image pinhole. The scan starts from the top left edge and ends on the bottom right edge as seen from the FPA (see Figure 3).
3. **Post-Processing consists in**:
    - Averaging multiple frames.
    - Determining the centroid of the imaged pinhole using the Otsu method [14].
    - Applying a correction to account for rotational displacement.
    - Computing the global distortion D of the UUT using the following formula:

$$D = \left(\frac{D_1 + D_2}{2 * D_{th}} - 1\right) \times 100 \tag{1}$$

Where D_1 and D_2 are the distances between the diametrically opposite and most remote locations of the centroids of the imaged pinholes, respectively on the diagonal and on the antidiagonal, measured in microns. D_{th} is the "theoretical" corresponding diagonal distance calculated from the appropriate angular positions of the UUT:

$$D_{th} = f \times \left(\sqrt{(tan(\theta_m - \theta_0) \quad + tan(\Theta_M - \theta_0))^2 + (tan(\phi_m - \phi_0) \quad + tan(\Phi_M - \phi_0))^2}\right) \tag{2}$$

Where:

- ϕ_m, θ_m, ϕ_M, θ_M correspond to the maximum angular positions of the rotation stage so that the pinhole is projected to every corner of the UUT sensor.
- (ϕ_0, θ_0) corresponds to the optical centre estimated from the barycentre of the farthest corners of the field of view.
- f is the focal length of the UUT and can be either the default focal length grabbed from the UUT information or an effective apparent focal length determined with another test by our software.

A distortion map is generated, overlaying a theoretical grid with measured centroid positions for precise distortion quantification (see Figure 4).

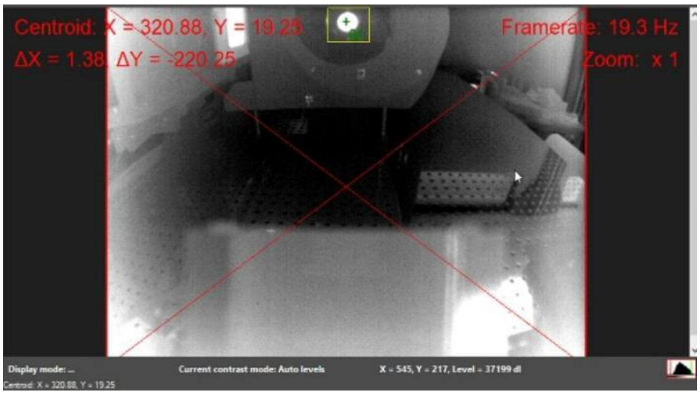

Figure 3. Screenshot of an infrared UUT frame grabbed during the distortion test measurement. The image of the projected pinhole can be seen on the top side of the frame. The centroid of the imaged pinhole is also shown.

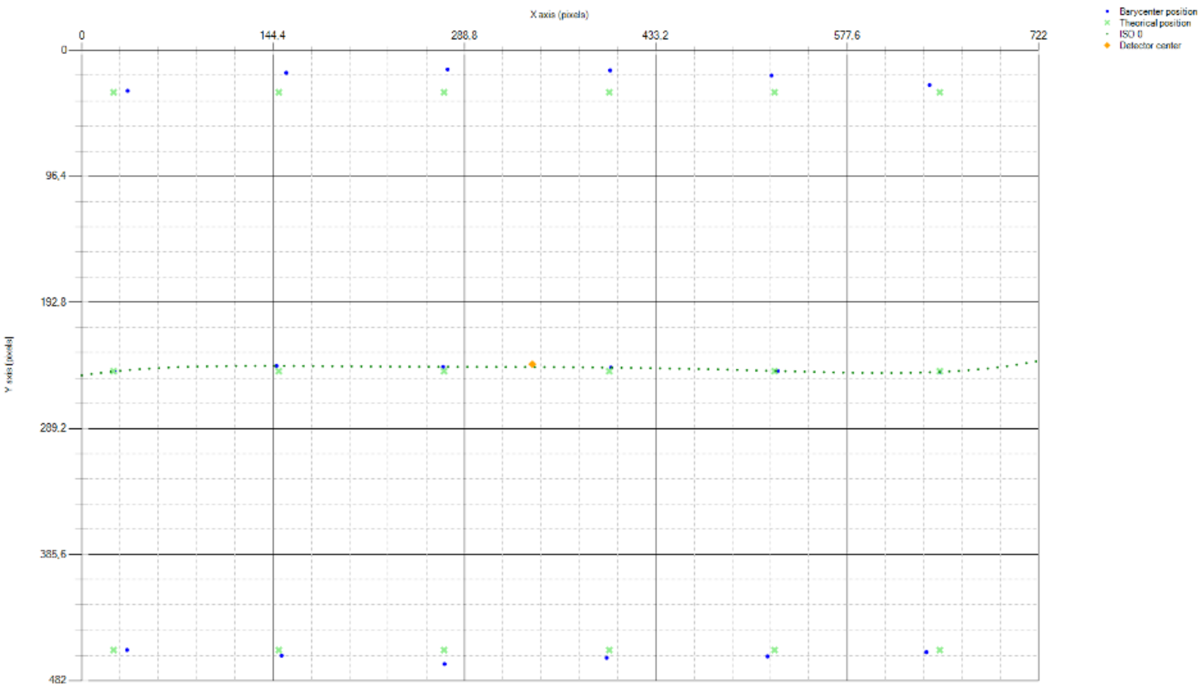

Figure 4. Distortion map obtained at the end of the test showing the differences between the theoretical locations of the projected pinholes patterns and the measured locations.

3. CORRECTION METHOD

Unlike traditional distortion measurement techniques relying on fixed grids, our system projects a pinhole at infinity while rotating the UUT. This introduces a non-linear displacement of the projected pinhole, necessitating correction before distortion calculation.

Our distortion test bench projects a pinhole pattern at infinity at different positions on the UUT. From the UUT point of view and even if the bench does not move, it looks as if the pinhole moves along the geodesics of a sphere and not along a plane as required for the distortion calculation. So, the pinhole image positions into the FPA plane have to be corrected.

The objective of the correction is to determine the projected position of the pinhole into the FPA plane of the UUT, i.e. into a local and rotating coordinate system,

Such a rotation implies a translation of the projected pinhole since it is projected at infinity. Because of the rotation, the displacement of the projected pinhole doesn't follow a regular linear translation. This implies the need to correct the coordinates of the localized centroids in the postprocessing step of the test, before calculating the distortion.

For that purpose, we model the setup as follows: the UUT is represented by an effective lens with focal length f, its optical centre corresponding to the origin O of a fixed 3D OXYZ orthonormal system, combined with a rectangular pixel grid representing the FPA. It is assumed in the below calculation that the UUT rotates around the optical centre O. Alternatively, we can see the FPA as a plane tangent to the sphere S of centre O and radius f. The FPA has itself a local 2D orthogonal system (**u, v**) with origin being P, the centre of the FPA. In the initial situation where there is no rotation, (φ=θ=0), the FPA lies in the plan x=-f, P is on the x-axis (see Figure 5 a)). As for the collimator, we model the projection of the pinhole as a dot projected at infinity, its parallel rays propagating along the x-axis.

For an arbitrary rotation (θ, φ) of the 2-axis rotation stage (see Figure 5b)), we note $A_{\theta,\varphi}$ the image of the pinhole on the FPA. With our representation, it corresponds therefore to the intersection between the x-axis (since the x-axis equals the optical axis of the system) and the FPA. θ stands for a rotation around the z-axis while φ around the y-axis. For φ=θ=0, $A_{0,0}$ = P. Note the convention of rotations. We chose the units of the two coordinate systems so that in the 3D fixed coordinate system, $||\vec{u}|| = ppx$ and $||\vec{v}|| = ppy$ where ppx and ppy are respectively the horizontal and vertical pixel pitch.

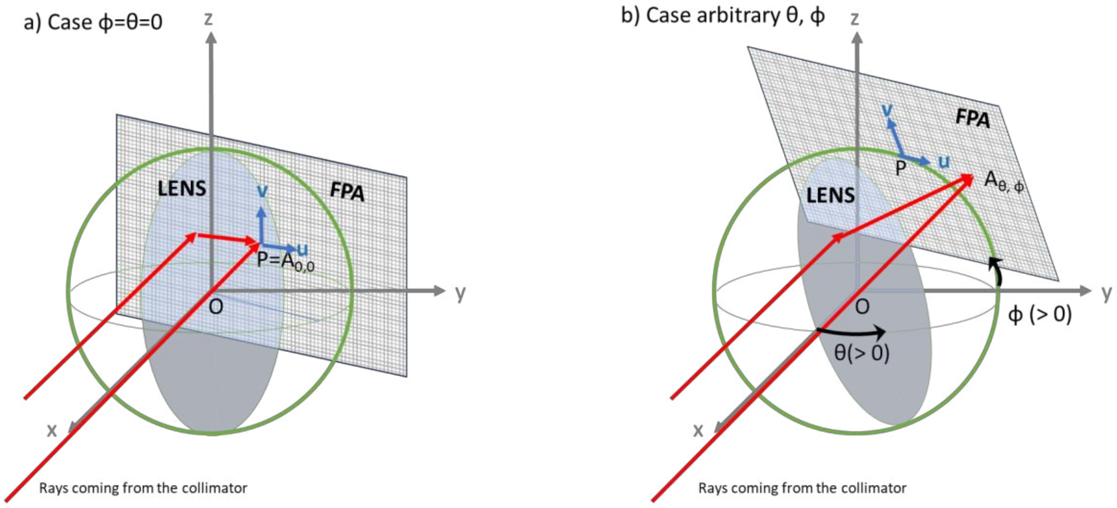

Figure 5. 3D representation of the mathematical model: the collimated radiation is directed towards the UUT along the x-axis where OXYZ is a fixed 3D orthonormal system. The UUT is modelled as the combination of an effective lens with focal length f centred on O, and an FPA rectangular grid whose centre is noted P and has a local coordinate system (**u, v**). (θ, φ) represents the rotation of the 2-axis stage around the z-axis and the y-axis. The FPA plane is tangent to the sphere of centre O and radius f.

Let's first determine the coordinates of $A_{\theta,\varphi}$ in the 3D fixed coordinate system for a given (θ, φ) position of the FPA. Let's consider the normalized vector $\vec{w}(\theta,\phi) = \frac{\overrightarrow{OP}}{||\overrightarrow{OP}||}$. This vector is normal to the FPA. The rotation of the UUT is first a rotation around the y-axis i.e. pitch (with an angle ϕ) followed by a rotation around the z-axis i.e. yaw (with an angle θ). So, $\vec{w}$ can be written as

$$\vec{w}(\theta,\phi) = R_z(\theta)R_y(\phi)\vec{w}(0,0) \tag{3}$$

where $R_i(\alpha)$ is the 3D rotation matrix of angle α around the i-axis. $\vec{w}(0,0)$ is simply equal to

$$\vec{w}(0,0) = \begin{pmatrix} 1 \\ 0 \\ 0 \end{pmatrix} \tag{4}$$

We can easily deduce the expression of $\vec{w}(\theta,\phi)$:

$$\vec{w}(\theta,\phi) = \begin{pmatrix} \cos(\theta) & -\sin(\theta) & 0 \\ \sin(\theta) & \cos(\theta) & 0 \\ 0 & 0 & 1 \end{pmatrix}\begin{pmatrix} \cos(\phi) & 0 & \sin(\phi) \\ 0 & 1 & 0 \\ -\sin(\phi) & 0 & \cos(\phi) \end{pmatrix}\vec{w}(0,0) = \begin{pmatrix} \cos(\theta)\cos(\phi) \\ \sin(\theta)\cos(\phi) \\ -\sin(\phi) \end{pmatrix} \tag{5}$$

The equation of the FPA is therefore

$$\cos(\theta)\cos(\phi).x + \sin(\theta)\cos(\phi).y - \sin(\phi).z = -f \tag{6}$$

So, we are now able to determine $A_{\theta,\varphi}$ in the 3D fixed system from Equation (6)

$$A_{\theta,\phi} = \begin{pmatrix} -\dfrac{f}{\cos(\theta)\cos(\phi)} \\ 0 \\ 0 \end{pmatrix} \tag{7}$$

Let's now find the coordinates of $A_{\theta,\varphi}$ in the local coordinate system. Since $\vec{u}$ and $\vec{v}$ follow the same rotation as in Equation (3) and since $\vec{u}(0,0) = \begin{pmatrix} 0 \\ ppx \\ 0 \end{pmatrix}$ and $\vec{v}(0,0) = \begin{pmatrix} 0 \\ 0 \\ ppy \end{pmatrix}$, we can deduce

$$\vec{u}(\theta,\phi) = \begin{pmatrix} -\sin(\theta).ppx \\ ppx.cos(\theta) \\ 0 \end{pmatrix} \tag{8}$$

And

$$\vec{v}(\theta,\phi) = \begin{pmatrix} \sin(\phi)\cos(\theta).ppy \\ ppy.sin(\phi)\sin(\theta) \\ ppy.\cos(\phi) \end{pmatrix} \tag{9}$$

With those two expressions in mind, and using Equation (7), we finally can deduce the local coordinates of $A_{\theta,\varphi}$:

$$A_{\theta,\phi} = \begin{pmatrix} \dfrac{f.tan(\theta)}{ppx.\cos(\phi)} \\ -f.\dfrac{\tan(\phi)}{ppy} \end{pmatrix} \tag{10}$$

This correction is applied to the positions of the projected pinhole centroids in the postprocessing as explained above.

4. MEASUREMENT ACCURACY

We follow a mathematical description of the uncertainty as recommended in [15] to estimate the measurement accuracy. Following the description of the distortion test procedure described in Section 2, we can explicit the computed distortion with the formula:

$$D = 100 \times \left[\frac{\sqrt{(x_m - x_M)^2 * ppx^2 + ((y_m - y_0)\cos(\theta_m - \theta_0) - (y_M - y_0)\cos(\theta_M - \theta_0))^2 * ppy^2}}{2f\sqrt{(\tan(\theta_m - \theta_0) + \tan(\theta_0 - \theta_M))^2 + (\tan(\phi_m - \phi_0) + \tan(\phi_0 - \phi_M))^2}} + \frac{\left[\sqrt{(x'_m - x'_M)^2 * ppx^2 + ((y'_m - y_0)\cos(\theta_m - \theta_0) - (y'_m - y_0)\cos(\theta_M - \theta_0))^2 * ppy^2}\right]}{2f\sqrt{(\tan(\theta_m - \theta_0) + \tan(\theta_0 - \theta_M))^2 + (\tan(\phi_m - \phi_0) + \tan(\phi_0 - \phi_M))^2}} - 1 \right] \quad (11)$$

where:

- x_m, y_m, x_M, y_M correspond to the coordinates of the centroids of the opposite imaged pinholes on a diagonal while x'_m, y'_m, x'_M, y'_M correspond to the ones on the antidiagonal

From equation (11) we can derive the standard uncertainty $u_c(D)$ by following the law of propagation of uncertainty [15]

$$u_c(D) = \sqrt{\sum_i \left(\frac{\partial g}{\partial x_i}\right)^2 u(\mathrm{x_i})^2} \quad (12)$$

Where x_i designate each of the above cited parameters and $u(x_i)$ their corresponding standard uncertainties. From there, the relative standard uncertainty $u_{r,c}(D)$ is given by:

$$u_{c,r}(D) = \frac{u_c(D)}{|D|} \quad (13)$$

The contributions from digitization conversions are neglected or digit displays. For practical evaluations, we can get a rough estimation by simplifying those calculations and making the following assumptions: uncertainties over the angular positions are the same, uncertainties over centroid localizations are the same, diagonal lengths are considered as equal to the longer ones, horizontal pitch is equal to the vertical pitch. And therefore, we obtain

$$u_{c,r}(D) \approx \sqrt{4\left(\frac{\mathrm{u}(\phi)}{\phi\sqrt{3}}\right)^2 + 4\left(\frac{\mathrm{u}(\mathrm{x})}{x\sqrt{3}}\right)^2 + \left(\frac{\mathrm{u}(\mathrm{f})}{f}\right)^2 + 2\left(\frac{\mathrm{u}(\mathrm{pitch})}{pitch}\right)^2} \quad (14)$$

A typical evaluation of uncertainty is now made for an uncooled LWIR sensor. In Table 1 presents the different parameters with values and uncertainties of the different contributors are given in the table below for an uncooled LWIR sensor equipped with a 50-degree FOV optics.

Table 1. Typical uncertainty contributions and their evaluations for distortion measurement of an uncool LWIR camera.

Contributor	Value	Uncertainty u
Location of the barycentre of the projected pinhole u(x)		+/- 0.5 px
Angular precision u(ϕ)		+/- 25 mdeg
Angular max rotation ϕ	+/- 25°	
Effective Focal length f of the UUT (f)	11 mm	0.2 %

FPA pitch (=ppx=ppy)	15 µm	negligeable
Dimensions (pixel)	640 x 480	

For this typical example, we get a relative uncertainty of $u_{c,r}(D) \approx 0.26\%$ showing the very high accuracy of our distortion test bench. Note that the given value uncertainty of the localization of the imaged pinhole centroid has been estimated empirically in typical cases. The estimation is likely to be overestimated since it is possible with this method to reach subscale precision as far as a couple of hundredths of pixels is considered for barycentre calculation[16].

The knowledge of the focal length of the UUT is obviously the main contributor of the uncertainty. And even, as this information is frequently unknown into manufacturers datasheet, the above 0.2% uncertainty is obtained through the measurement of the effective focal length, by measuring the magnification of a known square target using the same bench. If this contribution is excluded from the uncertainty of calculation, the uncertainty of distortion is 0.16%.

5. EXTENTION TO WINDOW DISTORTION MEASUREMENT

From a system point of view, thermal sensors or any imager are integrated in complete units like gimbals, infrared seekers of missiles, etc. In any case, such payloads are generally protected with a window (flat, curved, dome-type). The latter has naturally impacts on the performances of the sensor and the global optronics chain, for instance its MTF or its transmittance, especially in aeronautics [17], [18]. Some systems can measure some of those parameters [19] but not the distortion that can be crucial in applications like missile warning systems. It is especially true when the window is at grazing incidence with the sensor.

For that purpose, the bench is modified to handle such configuration (see Figure 6): we use two independent sets of 2-axis rotation stages, one for both the UUT and windows under test (WUT), and the other for the WUT only. Each set of rotation stages include two rotation axis stages (elevation and azimuth). Both are controlled by the home-made supervision monitoring software INFRATEST. The test allows thus to measure the distortion of the UUT for various relative positions of the WUT.

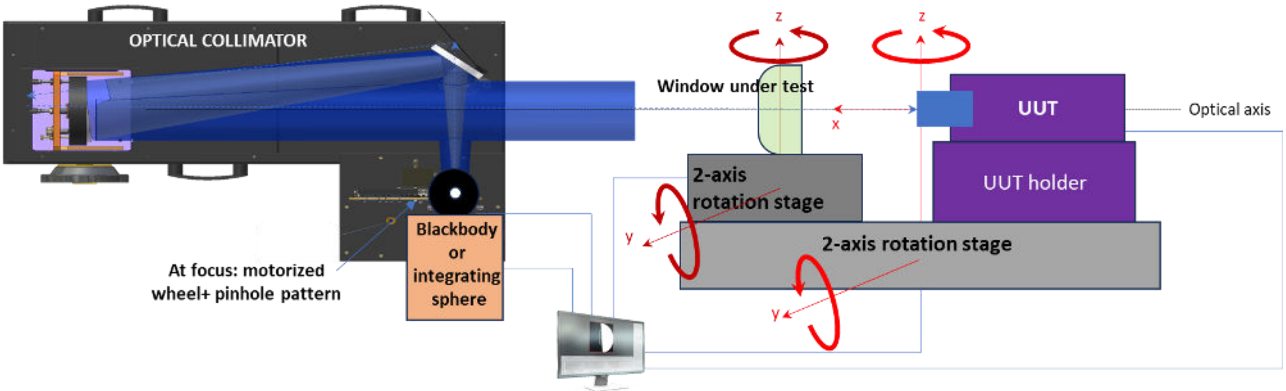

Figure 6. Schematics of the window distortion test bench. The collimated radiation emitted by an optical collimator, is sent to the UUT after going through the window under test (WUT). Both UUT and WUT are mounted on a motorized 2-axis rotation stage, the WUT itself is mounted on an independent 2-axis rotation stage.

As for the global relative combined uncertainty associated with this new setup, we have to take into account the second 2-rotation axis, resulting in roughly rewriting Equation (14)into

$$u_{c,r}(D) \approx \sqrt{6\left(\frac{\mathrm{u}(\phi)}{\phi\sqrt{3}}\right)^2 + 4\left(\frac{\mathrm{u}(\mathrm{x})}{x\sqrt{3}}\right)^2 + \left(\frac{\mathrm{u}(\mathrm{f})}{f}\right)^2 + 2\left(\frac{\mathrm{u}(\mathrm{pitch})}{pitch}\right)^2} \quad (15)$$

We assume the same uncertainties for the angular precisions. With a typical value of 0.06% for $\left(\frac{\mathrm{u}(\phi)}{\phi\sqrt{3}}\right)$, the contribution of the second stage remains very low.

6. CONCLUSIONS

We have developed a compact distortion test bench allowing user-friendly measurements of various optronics systems, from visible cameras up to longwave infrared thermal imagers. Based on a two-axis rotation stages of the UUT, this system allows to reach a very high accuracy typically as low as 0.2%. It can be extended to the measurement of the impact on distortion of a window or a dome placed in front of the UUT and mounted on a second two-axis rotation stage.

Ongoing work aims to enhance the system for fisheye and ultra-wide-angle cameras by incorporating fisheye-specific mapping functions into post-processing.

ACKNOWLEDGEMENTS

The authors thank M. de Masson d'Autume for fruitful discussions.

REFERENCES

[1] Brady, D. J.,Gehm, M. E., Stack, R. A., Marks, D. L., Kittle, D. S., Golish, D. R., Vera, E. M., and Feller, S. D., "Stack. multiscale gigapixel photography," Nature 486(7403), 386–389 (2012). https://doi.org/10.1038/nature11150
[2] Gerton, K. M., Novar, B. J., Brockmeier, W., and Putnam, C., "A novel Method for Optical Distortion Quantification," Optom. Vis. Sci. 96(2), 117-123 (2019). https://doi.org/10.1097/opx.0000000000001335
[3] Lin, J., Xing, M., Sha, D., Su, D., and Shen, T., "Distortion measurement of CCD imaging system with short focal length and large-field objective," Opt. Lasers Eng. 43(10), 1137-1144 (2005). https://doi.org/10.1016/j.optlaseng.2004.07.006
[4] ISO/TC 172/SC 1, "ISO 9039:2008 Optics and photonics – Quality evaluation of optical systems – Determination of distortion," Second edition, 2008. https://www.iso.org/standard/50090.html
[5] ISO/TC 42, "ISO 17850:2015 Photography – Digital cameras – Geometric distortion (GD) measurements," First edition 2015. https://www.iso.org/standard/60819.htm
[6] Li, X., Su, X., Hu, Z., Yang, L., Zhang, L., and Chen, F., "Improved distortion correction method and applications for large aperture infrared tracking cameras," Infrared Phys. Technol. 98, 82-88 (2019). https://doi.org/10.1016/j.infrared.2019.02.009
[7] Charbal, A., Dufour, J.-E., Guery, A., Hild, F., Roux, S., Vincent, L., and Poncelet, M., "Integrated Digital Image Correlation considering gray level and blur variations: Application to distortion measurements of IR camera," Opt. Lasers Eng. 78, 75-85 (2016). https://doi.org/10.1016/j.optlaseng.2015.09.011
[8] Wenzel, K. Abraham, Gy., Tamas, P., and Urbin, A., "Measurement of distortion using the Moire Interferometry," Optics 4(3-1), 14-17 (2015). https://doi.org/10.11648/j.optics.s.2015040301.14
[9] Yang, G., Miao, L., Zhang, X., Sun, C., and Qiao, Y., "High-accuracy measurement of the focal length and distortion of optical systems based on interferometry," Appl. Opt. 57(18), 5217 (2018). http://dx.doi.org/10.1364/AO.57.005217
[10] Wang, F., Zhang, Z., Wang, R., Zeng, X., Yang, X., Lv, S., Zhang, F., Xue, D., Yan, J., and Zhang, X., "Distortion measurement of optical system using phase diffractive beam splitter," Opt. Express 27(21), 29803-29816 (2019). https://doi.org/10.1364/OE.27.029803
[11] Miks, A., and Pokorny, P., "Use of diffraction grating for measuring the focal length and distortion of optical systems," Appl. Opt. 54(34): 10200-10206 (2015). https://doi.org/10.1364/AO.54.010200
[12] C. Barrat, et al., "Influence of ambient temperature on the radiation of IR reference sources: effect on the calibration of IR sensors and method of compensation," Proc. SPIE 10795, Electro-Optical and Infrared Systems: Technology and Applications XV, 107950M (2018). https://doi.org/10.1117/12.2325369
[13] Lardennois, M., Dorino, R., Bertaud, A., d'Autume, M., Arquetoux, G., Louboutin, A., Barrat, C., and Guider, R., "Design of a unique optical bench for complete performance characterization of night vision device", Proc. SPIE 12737, Electro-Optical and Infrared Systems: Technology and Applications XX, 127370F (2023). https://doi.org/10.1117/12.2680498

[14] Otsu, N, “A threshold selection method from gray-level histograms,” IEEE Trans Syst Man Cybern. 9(1), 62–66 (1979). https://doi.org/10.1109/TSMC.1979.4310076
[15] “Evaluation of measurement data – Guide to the expression of uncertainty in measurement,” JCGM100: 2008. First edition September 2008.
[16] Chen, M., Zhang, Z., Wu, H., Xie, S., and Wang, H., “Otsu-Kmeans gravity-based multi-spots center extraction method for microlens array imaging system,” Opt. Lasers Eng. 152, 106968 (2022). https://doi.org/10.1016/j.optlaseng.2022.106968
[17] Mathews, E., Wang, K., Meng W., and Jumper, E. J., "Turbulence scale effects and resolution requirements in aero-optics," Appl. Opt. 60, 4426-4433 (2021). https://doi.org/10.1364/ao.421304
[18] Chen, J., Tian, D., Jia, P., Wang, Z., Wang, Z., Xu, R., and Wang, Y., "Analysis of aero-optical effects within supersonic vehicle imaging fields," Opt. Express 33, 10262-10278 (2025). https://doi.org/10.1364/OE.553343
[19] Cabib, D., Rahav, A., and Barak, T., "Broad-band optical test bench (OPTISHOP) to measure MTF and transmittance of visible and IR optical components," Infrared Imaging Systems: Design, Analysis, Modeling, and Testing XVIII, Proc. of SPIE Vol.6543, 654311 (2007). http://dx.doi.org/10.1117/12.719170